Ultrasound in Med. & Biol., Vol. 33, No. 7, pp. 1086–1097, 2007

0301-5629/07/$–see front matter

ELSEVIER

doi:10.1016/j.ultrasmedbio.2007.01.009

● *Original Contribution*

REAL-TIME SHEAR VELOCITY IMAGING USING SONOELASTOGRAPHIC TECHNIQUES

KENNETH HOYT,* KEVIN J. PARKER,* and DEBORAH J. RUBENS†
*Department of Electrical and Computer Engineering, University of Rochester, Rochester, NY, USA; and †Department of Imaging Science, University of Rochester, Rochester, NY, USA

(*Received* 3 *July* 2006; *revised* 16 *October* 2006; *in final form* 16 *January* 2007)

Abstract—In this paper, a novel sonoelastographic technique for estimating local shear velocities from propagating shear wave interference patterns (termed crawling waves) is introduced. A relationship between the local crawling wave spatial phase derivatives and local shear wave velocity is derived with phase derivatives estimated using an autocorrelation technique. Results from homogeneous phantoms demonstrate the ability of sonoelastographic shear velocity imaging to quantify the true underlying shear velocity distributions as verified using time-of-flight measurements. Heterogeneous phantom results reveal the capacity for lesion detection and shear velocity quantification as validated from mechanical measurements on phantom samples. Experimental results obtained from a prostate specimen illustrated feasibility for shear velocity imaging in tissue. More importantly, high-contrast visualization of focal carcinomas was demonstrated introducing the clinical potential of this novel sonoelastographic imaging technique. (E-mail: hoyt@ece.rochester.edu) **© 2007 Published by Elsevier Inc. on behalf of the World Federation for Ultrasound in Medicine & Biology.**

Key Words: **Crawling waves, Elasticity imaging, Shear velocity estimation, Shear wave interference patterns, Sonoelastography.**

INTRODUCTION

Imaging the elastic properties of biological tissues has become the focal point of many research efforts (Gao et al. 1996; Ophir et al. 1999; Greenleaf et al. 2003). The universal goal of these initiatives revolves around mapping some tissue mechanical property in an anatomically meaningful manner to provide useful clinical information. Since changes in tissue stiffness are typically indicative of an abnormal pathologic process (Anderson and Kissane 1977), imaging parameters related to tissue elasticity may finally provide a gateway for differentiating normal from abnormal tissues.

For nearly two decades, elasticity imaging research has evolved into a diverse international endeavor with the majority of the efforts being founded on either ultrasound or magnetic resonance imaging system platforms. Ultrasound has the advantages of system mobility and real-time capability. Although all ultrasound-based elasticity imaging techniques are premised on the formation of elastic deformations in tissue, significant differences exist in the nature of the mechanical stimulus used to induce tissue motion and the subsequent acquisition and processing of tissue deformation data.

Vibrational sonoelastography is a tissue elasticity imaging technique that estimates the amplitude response of tissues under harmonic mechanical excitation using ultrasonic Doppler techniques (Lerner et al. 1988). Due to a mathematical relationship between particle vibrational response and received Doppler spectral variance (Huang et al. 1990), the amplitude of low frequency and low amplitude shear waves propagating in tissue can be visualized in real-time using sonoelastography to detect regions of abnormal stiffness (Parker et al. 1998). Compression elastography is another ultrasonic elasticity imaging technique that estimates soft tissue strain profiles owing to a quasistatic compressive force (Ophir et al. 1991; O'Donnell et al. 1994). In this particular method, strain is used as a surrogate for tissue stiffness; low tissue strain regions indicate high stiffness and *vice versa*. In contrast, acoustic radiation force-based methods utilize focused acoustical energy to induce localized tissue deformation, in effect remotely palpating deep soft tissue (Sugimoto et al. 1990). Using pulse echo ultrasound

Address correspondence to: Dr. Kenneth Hoyt, Department of Electrical and Computer Engineering, University of Rochester, 203 Hopeman Building, Rochester, NY 14627 USA. E-mail: hoyt@ece.rochester.edu

techniques, the elastic response of tissue following a high energy, focused acoustic pulse is estimated using either speckle tracking (Nightingale et al. 2001; Lizzi et al. 2003; Bercoff et al. 2004) or Doppler techniques (Barannik et al. 2002). These approaches analyze the mechanical response of tissue to acoustic radiation forces by imaging either the temporal displacement and relaxation (function of viscoelastic properties) at the focus or the spatial propagation of induced shear waves (related to shear modulus distribution). Transient elastography is another elasticity imaging technique that functions by inducing propagating shear waves using pulsed acoustic radiation forces whereby tissue displacements are tracked using an ultrafast ultrasound scanner (5 to 10,000 frames per s) (Bercoff et al. 2004). Subsequently, tissue displacement estimates are imaged allowing visualization of shear waves as they propagate across the image plane. A variant of radiation force-based elasticity imaging is that termed vibro-acoustography (Fatemi et al. 1998; Greenleaf et al. 2003). In this technique, a low frequency (in the kHz range) dynamic radiation force is produced by two confocal continuous-wave ultrasound beams transmitting at offset frequencies. Since the oscillating force vibrates the tissue at the focal region and produces an acoustic emission, an image depicting the elastic response is formed by spatially translating the focal point within the object and collecting the resultant acoustic emissions using a sensitive hydrophone.

In a recent discovery by Wu et al. (2004), it was found that interfering shear waves could produce slowly propagating interference patterns with an apparent velocity much less than (but proportional to) the underlying true shear velocity. Termed crawling waves, they are generated using a pair of mechanical sources vibrating at slightly offset frequencies. More importantly, these shear wave (interference) patterns can be visualized in real-time using sonoelastographic imaging techniques. In general, crawling wave images describe shear wave propagation patterns and allow for estimation of the spatial elastic properties in tissue, namely, shear velocity distributions.

Utilizing a local frequency estimator (LFE), (Knutsson et al. 1994; Manduca et al. 1996), Wu et al. (2004) showed that qualitative images describing shear velocity distributions can in fact be generated from crawling wave image sequences. One disadvantage to the LFE-based approach to sonoelastographic crawling wave analysis is that it requires amplitude normalization and detrending to avoid spectral leakage artifacts and subsequent image degradation. Alternatively, McLaughlin et al. (2006) have developed a technique whereby distinctive features of the crawling waves are identified and arrival times at points in the image plane are calculated. Since these features move in accord with the underlying true shear velocity distribution, quantitative estimates of local shear velocity are obtained and imaged. Although preliminary results using this approach in phantoms are promising, the mathematical complexity currently rules out real-time clinical applications.

In this paper, we expand the crawling wave phenomena and introduce a novel shear velocity estimation and imaging technique. Given a sonoelastographic crawling wave image frame, a 1D kernel window is translated across a region-of-interest in the direction of shear wave propagation with local shear velocity estimates computed using an autocorrelation-based algorithm (as a function of spatial position). Upon completing this process for each range location, the resultant image describes the 2D spatial shear velocity distribution. One of the main advantages of the novel shear velocity estimation technique introduced in this paper relates to computational simplicity. Due to the undemanding numerical structure, real-time sonoelastographic shear velocity imaging is deemed feasible.

The goal of this work was to present initial results using this novel sonoelastographic shear velocity imaging technique. Following a mathematical derivation of the shear velocity estimation and imaging method, simulation results explain the trade-offs between various system level and image processing parameters. Experimental results in tissue-mimicking phantoms illustrate the ability of this imaging technique to accurately describe the true shear velocity distributions. Lastly, experimental results obtained from a prostate specimen introduce feasibility for sonoelastographic shear velocity imaging in tissue.

THEORY

Fundamentals of tissue elasticity

We begin by expressing the wave motion equation for a linear and isotropic medium in terms of the displacements as:

$$\frac{E}{2(1+\nu)}\nabla^2\bar{u} + \frac{E}{2(1+\nu)(1-2\nu)}\nabla\nabla\cdot\bar{u} = \rho\frac{\partial^2\bar{u}}{\partial t^2}, \quad (1)$$

where E, ν, ρ, $\bar{u}$ and t are the Young's modulus, Poisson's ratio, mass density, displacement vector and time variable, respectively. Equation 1 can be decomposed into two decoupled motion equations, one governing longitudinal wave motion and the other governing shear wave motion (Landau and Lifshitz 1986). Only the shear wave equation is chosen for consideration for the following reasons. First, the longitudinal waves have wavelengths much larger than organs of interest at the frequencies

used in sonoelastography (Parker et al. 1992). Additionally, biological tissues are nearly incompressible, so the Poisson's ratio approaches 0.5 (Fung 1981; Parker et al. 1990). At this Poisson's ratio, the wave dilation representing the longitudinal wave motion is close to zero. Thus, the shear wave motion $\bar{u}_S$ dominates the wave propagation. In a homogeneous medium, the shear wave component is described by the wave equation (Landau and Lifshitz 1986):

$$\nabla^2 \bar{u}_S - \frac{1}{c_S^2} \frac{\partial^2 \bar{u}_S}{\partial t^2} = 0, \tag{2}$$

where c_S denotes the shear wave velocity expressed as:

$$c_S = \sqrt{\frac{E}{2\rho(1+\nu)}}. \tag{3}$$

Furthermore, if we consider propagating shear waves in soft tissue (*i.e.*, incompressible medium) then eqn 3 can be further simplified to:

$$c_S = \sqrt{\frac{E}{3\rho}}, \tag{4}$$

which relates the shear wave velocity to the Young's modulus and mass density of a homogeneous tissue sample.

Sonoelastographic imaging

In sonoelastography, a low frequency (50 to 400 Hz) and low amplitude (20 to 100 μm) mechanical vibration is employed to noninvasively excite shear waves in tissue. Assuming that the external vibration has harmonic temporal and spatial dependence (and neglecting attenuation), the resulting shear wave displacement vector can be expressed as:

$$u_S = u \exp(ik_S x + i\omega_S t), \tag{5}$$

where u is the vibration amplitude of the displacement field, ω_S is the angular vibration frequency and k_S represents the shear wave number. Premised on the tissue response from propagating shear waves, elasticity information can be estimated in depth using Doppler ultrasonic techniques. Specifically, the Doppler shift of an ultrasonic wave scattered from a spatially oscillating object (tissue volume) is given by a Fourier-Bessel series of equally spaced harmonics above and below the Doppler carrier frequency (Huang et al. 1990). It has been shown that the vibrational amplitude of tissue scatterers in sinusoidal motion alters the power spectrum of an insonifying ultrasound beam in a predictable manner. In particular, a linear relationship exists between the vibrational amplitude u and the standard deviation of the power spectrum σ as follows (Huang et al. 1990):

$$\sigma = \sqrt{2} \frac{u \omega_S \omega_L}{c_L}, \tag{6}$$

where ω_L is the radian frequency of the ultrasound wave and c_L is the longitudinal wave velocity in the material being imaged (assumed constant at 1540 m/s). Equation 6 forms the basis of sonoelastographic imaging. Using a modified pulsed Doppler ultrasound system, local estimates of tissue elasticity can be estimated and imaged in real-time to reflect changes in deep tissue stiffness (Parker et al. 1998). In practice, when a region-of-tissue contains a stiff lesion or mass, a local decrease in peak vibrational amplitude results. The interested reader is referred to Taylor et al. (2000) for a comprehensive description of the Doppler signal processing techniques utilized in real-time sonoelastographic imaging.

Shear wave interference patterns

We begin by considering two (equal amplitude) shear wave excitation sources positioned transversely on opposite sides of a medium and separated by distance D. Note that in the equations to follow, shear wave excitation source one and two are located at positions $-D/2$ and $D/2$, respectively. If one of the two sources vibrates at frequency ω_S and the other source vibrates at $\omega_S + \Delta\omega_S$, where $\Delta\omega_S \ll \omega_S$, then the propagating shear waves can be expressed as follows (Wu et al. 2004):

$$u_1(x,t) = A \exp\left[-\alpha\left(x + \frac{D}{2}\right)\right] \exp\left[ik_S\left(x + \frac{D}{2}\right) + i\omega_S t\right], \tag{7}$$

$$u_2(x,t) = A \exp\left[-\alpha\left(\frac{D}{2} - x\right)\right] \exp\left[i(k_S + \Delta k_S)\left(\frac{D}{2} - x\right) + i(\omega_S + \Delta\omega_S)t\right], \tag{8}$$

where u_1 and u_2 are the instantaneous right and left propagating waves, respectively, A is the source amplitude, α is the shear wave attenuation coefficient, Δk_s is the shear wave number difference and x is the spatial variable (parallel to the propagating shear wave axis). The interference pattern U is the superposition of the two waves described by eqn 7 and eqn 8:

$$U(x,t) = u_1(x,t) + u_2(x,t), \tag{9}$$

and describes the coupled shear wave displacement field (neglecting boundary reflections). It is important to note

that if the shear wave sources are far away compared with the size of the field of view, then the waves from each source can be considered plane waves (Wu et al. 2006). Thus, eqn 9 may be expressed as:

$$U(x, y, t) = u_1(x, t) + u_2(x, t). \tag{10}$$

where y is the spatial variable orthogonal to the shear wave propagation axis. Equation 10 indicates that for a homogeneous medium the shear wave interference patterns can be regarded as a set of harmonic signals independent of the y-dimension. Furthermore, owing to the frequency difference between the sources, the shear wave interference patterns move slowly toward the source with the lower frequency and at an apparent velocity equal to $\Delta\omega_S/2\omega_S{*}c_s$ (Wu et al. 2004). These propagating shear wave interference patterns have been appropriately termed crawling waves.

In sonoelastography, it is the magnitude of a vibrating target that is imaged. Therefore, eqn 10 is expressed alternatively as:

$$\left|U(x, y, t)\right|^2 = \left[u_1(x, t) + u_2(x, t)\right] * \left[u_1^*(x, t) + u_2^*(x, t)\right], \tag{11}$$

where u^* is the complex conjugate of u and the squared operator is used to recover a mathematical expression for a harmonic signal. Inserting eqn 7 and eqn 8 into eqn 11 and simplifying the expression yields the following:

$$\left|U(x, y, t)\right|^2 = 2A^2\exp(-\alpha D)\left[\cosh(2\alpha x) + \cos(2k_S x + \Delta k_S x + \Delta\omega_S t)\right]. \tag{12}$$

Inspection of the right-hand harmonic term reveals that the spatial frequency of the shear wave interference pattern is approximately twice the frequency of the vibrating sources. Finally, sampling of the crawling wave displacement field described by eqn 12 results in the following digitized signal:

$$s(m, n, r) = 2A^2\exp(-\alpha D)\left[\cosh(2\alpha m T_m) + \cos(2k_S m T_m + \Delta k_S m T_m + \Delta\omega_S r T_r)\right], \tag{13}$$

where m, n and r are integer values, T_m denotes the spatial sampling interval along the shear wave propagation axis and T_r is the temporal sampling interval (typically referred to as the frame rate).

Shear velocity estimation

In regards to eqn 13, the shear wave velocity can be found by taking the spatial derivative of the phase argument along the shear wave propagation axis (assumed to be m) as follows:

$$\frac{\partial\phi}{\partial m} = \frac{\partial(2k_S m T_m + \Delta k_S m T_m)}{\partial m} = (2k_S + \Delta k_S)T_m \tag{14}$$

By noting the following expressions:

$$k_S = \frac{2\pi f_S}{c_S},$$

and

$$\Delta k_S = \frac{2\pi\Delta f_S}{c_S},$$

where $f_S = \omega_S/2\pi$ and $\Delta f_S = \Delta\omega_S/2\pi$, then eqn 14 can be rewritten as a function of the shear velocity:

$$\frac{\partial\phi}{\partial m} = \frac{2\pi(2f_S + \Delta f_S)T_m}{c_S}. \tag{15}$$

Typically, only discrete spatial data are available for analysis and this implies that only an approximation to the derivative in eqn 15 can be computed. One common approach to this estimation problem is the autocorrelation-based technique described by Kasai et al. (1985). For the interested reader, a more elaborate description of Kasai's estimator can be found in Jensen (1996). However, this approach requires complex data sequences. Considering the discrete-time displacement field described by eqn 13, the analytic shear wave displacement field s_A can be accurately computed using fast Fourier transform (FFT) techniques (Marple 1999). Therefore, using a kernel widow size of N data samples the normalized autocorrelation function at lag 1 can be approximated as:

$$\hat{R}(1) = \frac{1}{N-1}\sum_{z=1}^{N-1} s_A^*(z)s_A(z+1), \tag{16}$$

where the data segment is taken parallel to the crawling wave propagation axis. Given the discrete autocorrelation estimates of eqn 16, the phase derivative is described as follows:

$$\frac{\partial\phi}{\partial m} = \tan^{-1}\left[\frac{\Im\left\{\hat{R}(1)\right\}}{\Re\left\{\hat{R}(1)\right\}}\right], \tag{17}$$

where $\Im\{\bullet\}$ and $\Re\{\bullet\}$ denotes the imaginary and real parts, respectively. Combining eqn 17 and eqn 15 and rearranging the terms results in the following expression:

Table 1. Default values used for simulation studies

Parameter	Value
Vibration source seperation (D)	50 mm
Attenuation coefficient	0.25 cm^{-1}
Vibration frequency (f)	200 Hz
Spatial sampling interval (T_n)	0.4 mm
Quantization levels (Q_{LVL})	8-bit
Signal-to-noise ratio (SNR)	30 dB
Kernel size (N)	16 samples

$$c_S = \frac{2\pi(2f_S + \Delta f_S)T_m}{\tan^{-1}\left[\frac{\Im\{\hat{R}(1)\}}{\Re\{\hat{R}(1)\}}\right]}, \quad (18)$$

which indicates that the shear velocity can be estimated from the spatial interference (or crawling wave) patterns given *a priori* knowledge of the source vibration frequencies and spatial sampling rate. In practice, a kernel window of length N is translated across the image plane (or region-of-interest) in the direction of shear wave propagation with local shear velocity estimates obtained for each spatial position using eqn 18. The resultant data matrix is imaged and describes the 2D spatial shear velocity distribution. One of the main advantages to the shear velocity estimation technique described above relates to computational simplicity. Due to the undemanding numerical structure (comparable to conventional Doppler color flow processing), real-time sonoelastographic imaging of shear velocity distributions is deemed feasible.

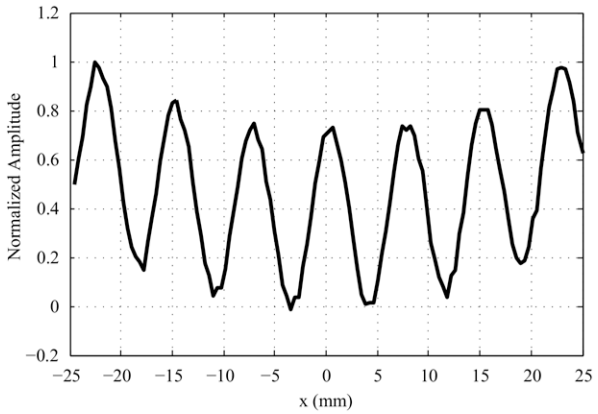

Fig. 1. Simulated shear wave interference pattern (*i.e.*, one-dimensional displacement vector) for a pair of coherent excitation sources separated laterally by a distance of 50 mm and vibrating at 200 Hz. A shear wave attenuation of 0.25 cm^{-1} was assumed.

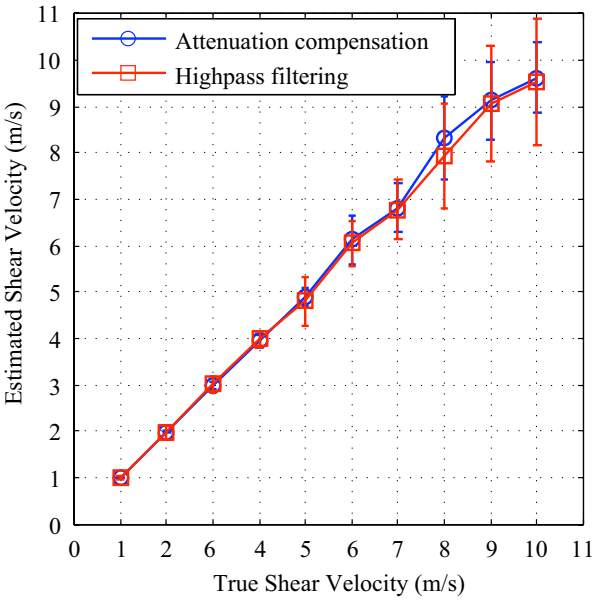

Fig. 2. Estimated vs. true shear velocity response in simulation for attenuation compensation via amplitude normalization and highpass spatial filtering.

SIMULATIONS

Methods

To evaluate the new shear velocity estimation technique, a 1D sonoelastographic simulation program was developed using Matlab 7.0 (Mathworks, Inc., Natick, MA, USA). The model assumes plane wave conditions

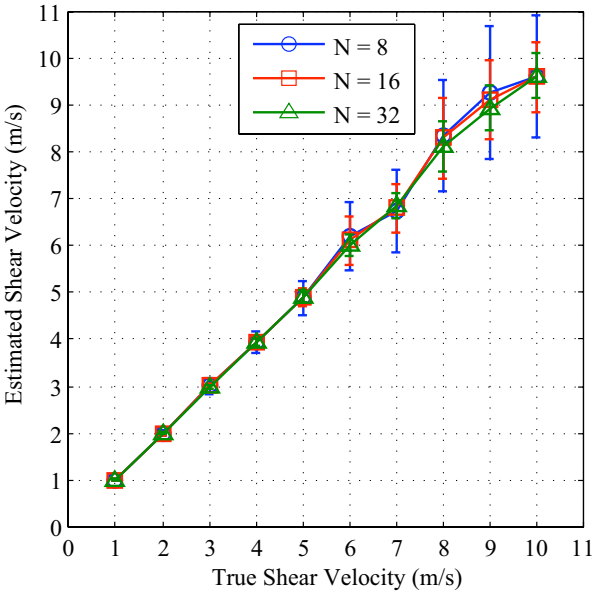

Fig. 3. Estimated vs. true shear velocity response in simulation for kernel window sizes of 8, 16 and 32 samples.

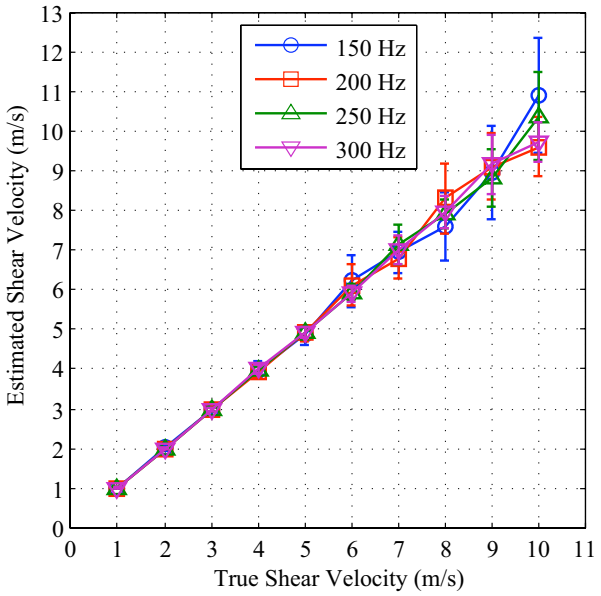

Fig. 4. Estimated vs. true shear velocity responses in simulation plotted as a function of the vibration frequency, namely, 150, 200, 250 and 300 Hz.

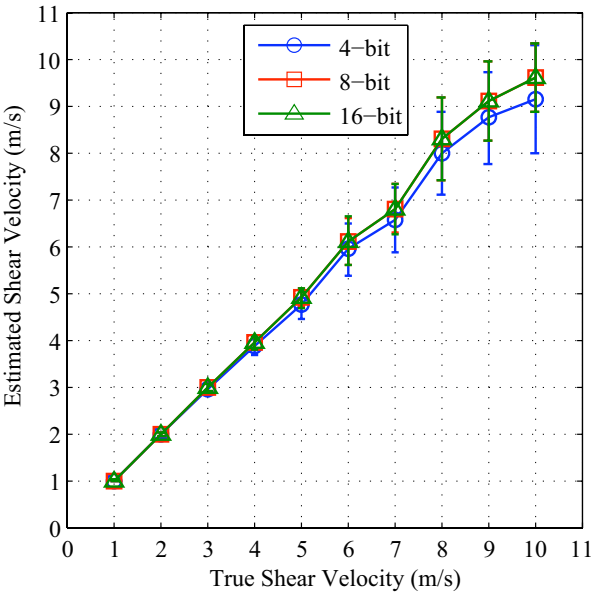

Fig. 6. Estimated vs. true shear velocity responses in simulation plotted as a function of intensity quantization levels, namely, 4, 8 and 16-bit.

and that the instantaneous shear wave interference patterns (*i.e.*, shear wave displacement vector) propagating in a locally homogeneous and isotropic medium can be described by eqn 13. Without loss of generality, we set Δk in eqn 13 to zero, which is indicative of a static shear wave interference pattern possessing the same intrinsic tissue elasticity information as the crawling wave case (Wu et al. 2004). For all results the shear wave signal-to-noise ratio (*SNR*) was implemented by superimposing white Gaussian noise (at the specified level) onto the simulated shear wave interference patterns. All shear velocity estimates were computed using eqn 18 and plotted as a function of the true shear velocity values

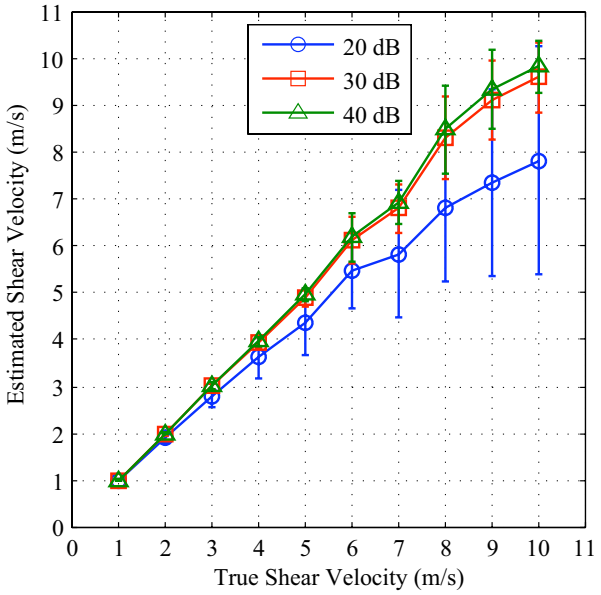

Fig. 5. Estimated vs. true shear velocity responses in simulation plotted as a function of shear wave signal-to-noise ratio (SNR), namely, 20, 30 and 40 dB.

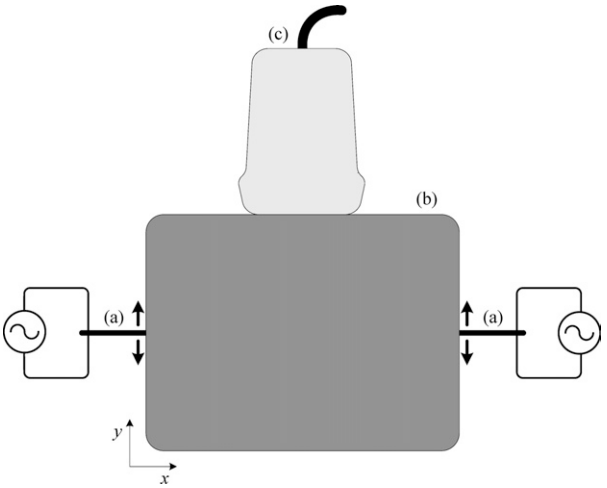

Fig. 7. Illustration of experimental set-up used to produce crawling waves in phantoms. Two piezoelectric shear wave sources (a) are in contact with the phantom (b) with arrows indicating the motion vectors. Shear wave displacement fields are imaged using an ultrasound probe (c) as they propagate into the medium.

used to simulate the displacement fields. Statistical results in simulation were computed from 25 independent realizations. Default simulation parameters are listed in Table 1 unless otherwise stated.

Results

A typical simulated shear wave interference pattern is illustrated in Fig. 1. Specifically, the shear velocity of the material was assumed to be 3 m/s and the wavelength was measured to be 7.5 mm, indicating that the spatial frequency is 400 Hz. Hence, the spatial frequency is twice the source excitation frequencies with the interference pattern superimposed on a hyperbolic cosine function. The effect of this hyperbolic profile is a biasing of the shear velocity estimates since it effectively introduces a low frequency signal component. Therefore,

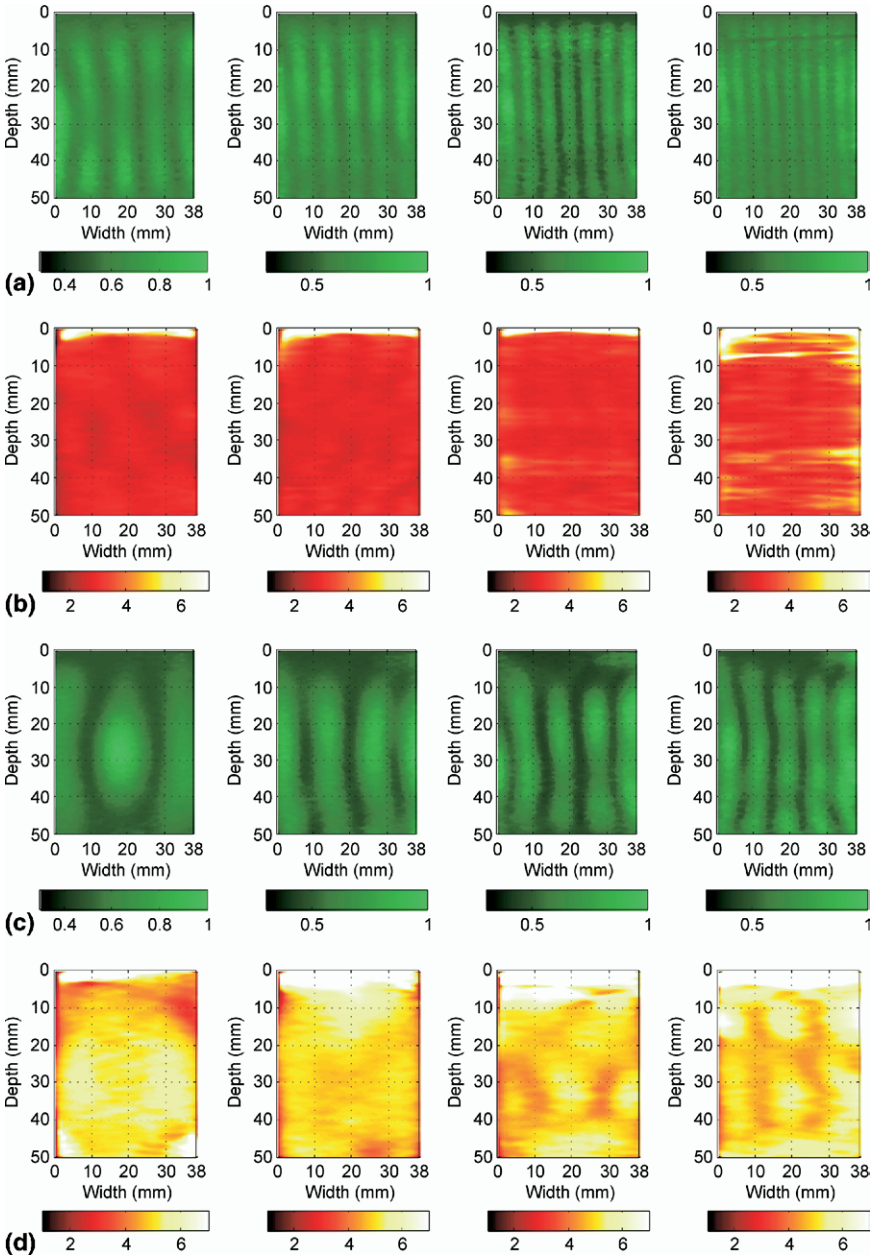

Fig. 8. Experimental shear wave interference pattern results using homogeneous phantoms of relatively (a) low and (c) high elastic moduli (using shear wave vibration frequencies of 150, 200, 250 and 300 Hz, left to right, respectively). The matched shear velocity images (units of m/s) are depicted in (b) and (d), respectively. Notice that an increase in the material elastic modulus corresponds to an increase in shear velocity estimates and is independent of vibration frequency.

attenuation compensation via highpass spatial filtering or amplitude normalization using eqn 13 must be employed to maximize shear velocity estimator performance. Regarding the former, filtering is performed by suppressing the first two Fourier series coefficients when computing the analytic data sets and before shear velocity estimation. Results demonstrating both attenuation compensation approaches are illustrated in Fig. 2. As illustrated, shear velocity estimates closely match that of the true shear velocity in the range of 1 to 10 m/s albeit the filtering approach to attenuation compensation produces more estimation variability for higher shear velocities. Consequently, attenuation compensation using amplitude normalization will be utilized for all simulation results to follow.

The effect of kernel size on shear velocity estimates is illustrated in Fig. 3. Note that kernel size is analogous to packet size or ensemble length in conventional Doppler color flow imaging. As the results demonstrate, increasing the kernel window size reduces estimator variability. Since shear velocity estimates are obtained by spatially translating the kernel window throughout the region-of-interest, a fundamental trade-off exists in that increasing the window size to minimize estimator variance decreases the spatial resolution. The results of Fig. 4 describe the effects of vibration frequency on shear wave velocity estimator performance. Notice that as the source vibration frequency is increased, the shear velocity estimates exhibit less variability because for a given kernel window size more waveform activity is observed. In practice, higher vibration frequencies are more attenuated effectively reducing the *SNR*. Therefore, the results of Fig. 5 illustrate the effect of shear wave *SNR* on shear velocity estimator performance. As the signal noise levels increase, there is a corresponding degradation in estimator performance. Specifically, simulation results demonstrate that for a 20 dB noise level, the shear velocity estimates tend to underestimate the higher true shear velocities in addition to exhibiting unacceptable levels of variability. Hence, maximizing the shear wave *SNR* is of paramount importance. In practice, this can be accomplished by increasing the vibrational amplitude of the shear wave excitation sources.

The number of quantization levels for any given imaging technique determines the display resolution. The role of quantization on shear velocity estimator performance in depicted in Fig. 6. Although 4-bit amplitude quantization introduces a relatively higher degree of variance on the shear velocity estimates compared with that obtained using both 8-bit and 16-bit quantized data, the latter two demonstrate comparable results. Since lower quantization levels are associated with higher levels of quantization noise, it is shown that minimizing this noise source has inherent advantages on estimator performance.

EXPERIMENTS

Methods

In the validating experiments, two bending piezoelectric elements termed biomorphs (Piezo Systems, Cambridge, MA, USA) are applied as the vibration sources. A dual channel signal generator (Model AFG320, Tektronix, Beaverton, OR, USA) produces two monochrome low frequency signals that are slightly offset (typically less than 0.5 Hz). These signals are passed through a two channel amplifier before being input to the biomorphs. A LOGIQ 9 scanner (General Electric Medical Systems, Milwaukee, WS, USA) that has been modified for sonoelastography was used with a M12L linear array probe (5 to 13 MHz bandwidth) for real-time visualization of the propagating crawling waves (*i.e.*, shear wave interference pattern motion). The frame rate for the sonoelastographic system is typically greater than 12 frames per s and dependent on the scanning field of view. This unit allows access to the demodulated data sets that were stored and transferred to an external computer for processing. A schematic drawling of the experimental set-up is illustrated in Fig. 7.

In the first set of experiments, two homogeneous tissue mimicking phantoms (10 × 10 × 10 cm) of

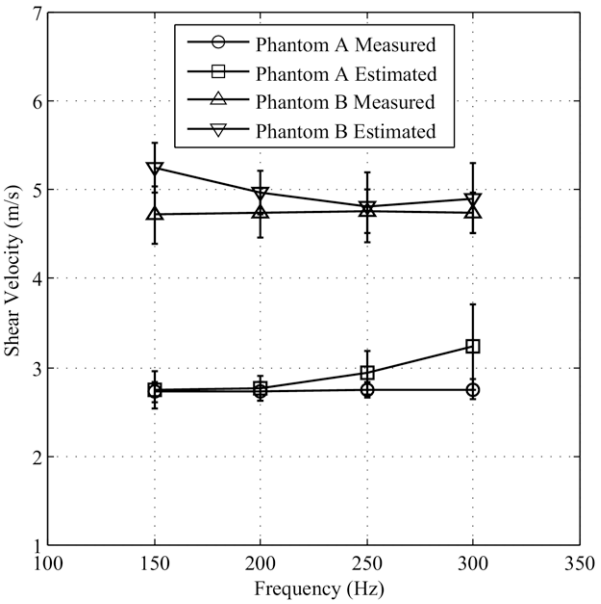

Fig. 9. Matched shear velocities as estimated from sequences of shear wave interference sonoelastograms and sets of physical measurements (*i.e.*, time-of-flight). Statistical results were acquired as a function of shear wave vibration frequency and from the relatively soft (Phantom A) and hard (Phantom B) homogeneous phantoms.

different stiffness were evaluated. Shear wave velocities for the two respective phantoms were estimated using time-of-flight methods (Wu et al. 2004). The purpose of this experimental component was to assess and compare shear velocity imaging results to measured values. In the second experiment, a heterogeneous tissue mimicking phantom (13 × 13 × 8 cm) containing a 1 cm (in diameter) stiff circular inclusion was utilized for a preliminary assessment of shear velocity image contrast. Mechanical measurements were performed on both background and inclusion samples to obtain elastic modulus values (Taylor et al. 2001) where the elastic modulus is related to the shear velocity via eqn 3. Note we assume a mass density of the tissue-mimicking samples equal to that of water. Phantoms were gelatin-based and made using techniques described previously by Hall et al. (1997). For all experimental scans, a sequence of 25 crawling wave sonoelastograms was obtained and the corresponding shear velocity images were generated and averaged. Image regions were analyzed for statistical purposes.

Finally, the proposed imaging technique was used to obtain a sonoelastographic shear velocity image from an excised prostate gland obtained immediately following radical prostatectomy on a 55-y-old patient. The excised specimen was embedded in an agar mold (Taylor et al. 2005) and, subsequently, imaged using the same experimental set-up described above for the phantom studies. The final diagnosis was obtained from the surgical pathology report. The prostate was chosen as a target organ because of its clinical significance and for our goal of visualizing focal lesions in tissue using sonoelastographic methods. Note that tissue specimen use was approved by our institutional review board and was compliant with the Health Insurance Portability and Accountability Act (HIPAA). Informed consent was obtained for the use of the excised gland.

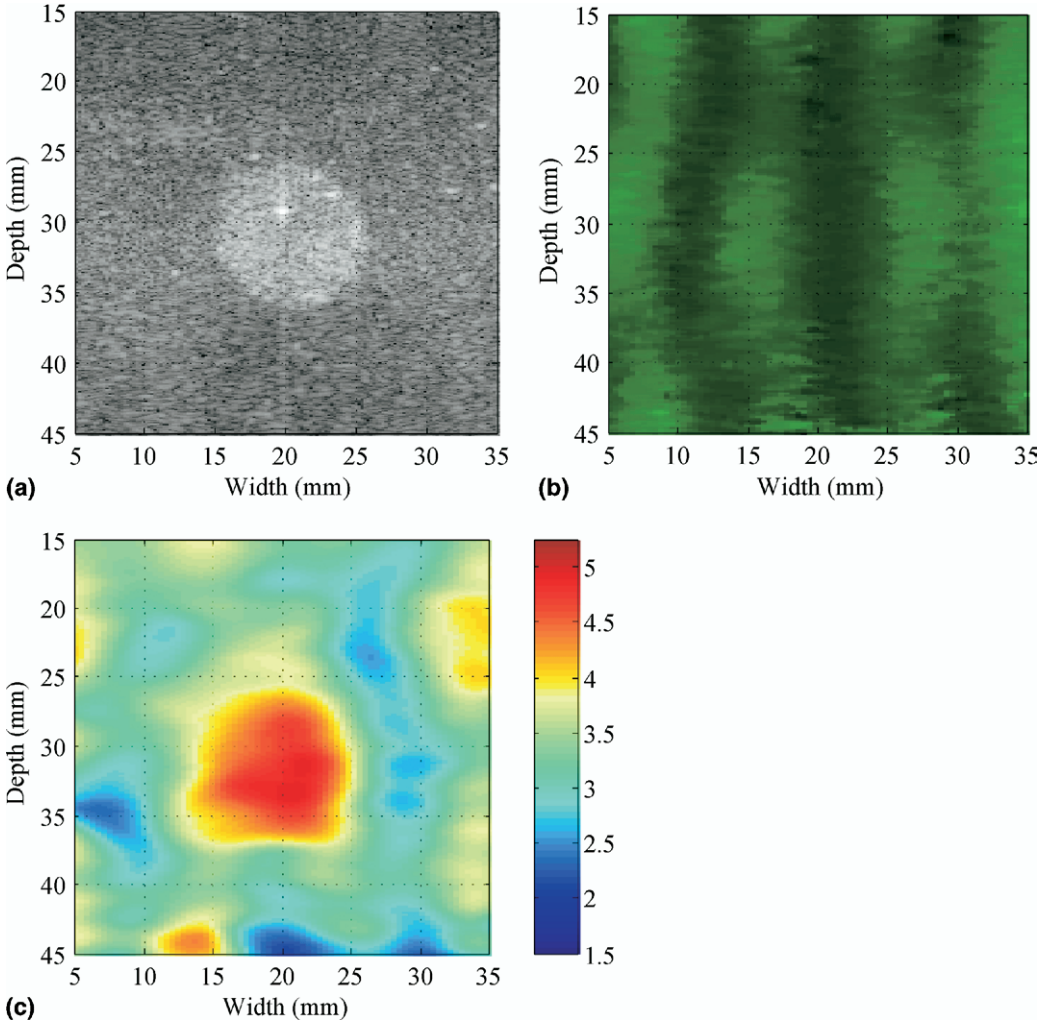

Fig. 10. Experimental crawling wave results using heterogeneous phantom and vibration sources of 200 and 200.15 Hz. Results depict the matched (a) B-mode ultrasound image, (b) Sonoelastogram and (c) Shear velocity images (units of m/s).

For all experimental results, shear wave attenuation effects were minimized by suppressing the first two Fourier series coefficients when computing the analytic image sets and before shear velocity estimation. This approach is analogous to highpass filtering and is implemented efficiently.

Results

The results of Fig. 8 illustrate the crawling wave sonoelastograms and matched shear velocity images for the two homogeneous phantoms. For a given vibration frequency, the spatial frequency of the harder phantom (Fig. 8c) is lower compared with the softer phantom (Fig. 8a), thus, indicating an increase in the true shear velocity distribution. Corresponding shear velocity images for the soft and hard phantoms are depicted in Fig. 8b and d, respectively. Notice that an increase in phantom stiffness corresponds to an increase in shear velocity estimates and is independent of vibration frequency, although at higher vibration frequencies, the shear velocity images exhibit artifacts that are attributed to increased attenuation effects that were not compensated for using amplitude normalization. Statistical results were obtained from these phantoms and compared with measured shear velocities, Fig. 9. As these results demonstrate, the shear velocity images closely match the true distribution, across a range of frequencies from 150 to 300 Hz.

Results from the heterogeneous phantom are illustrated in Fig. 10. Although not evident from crawling

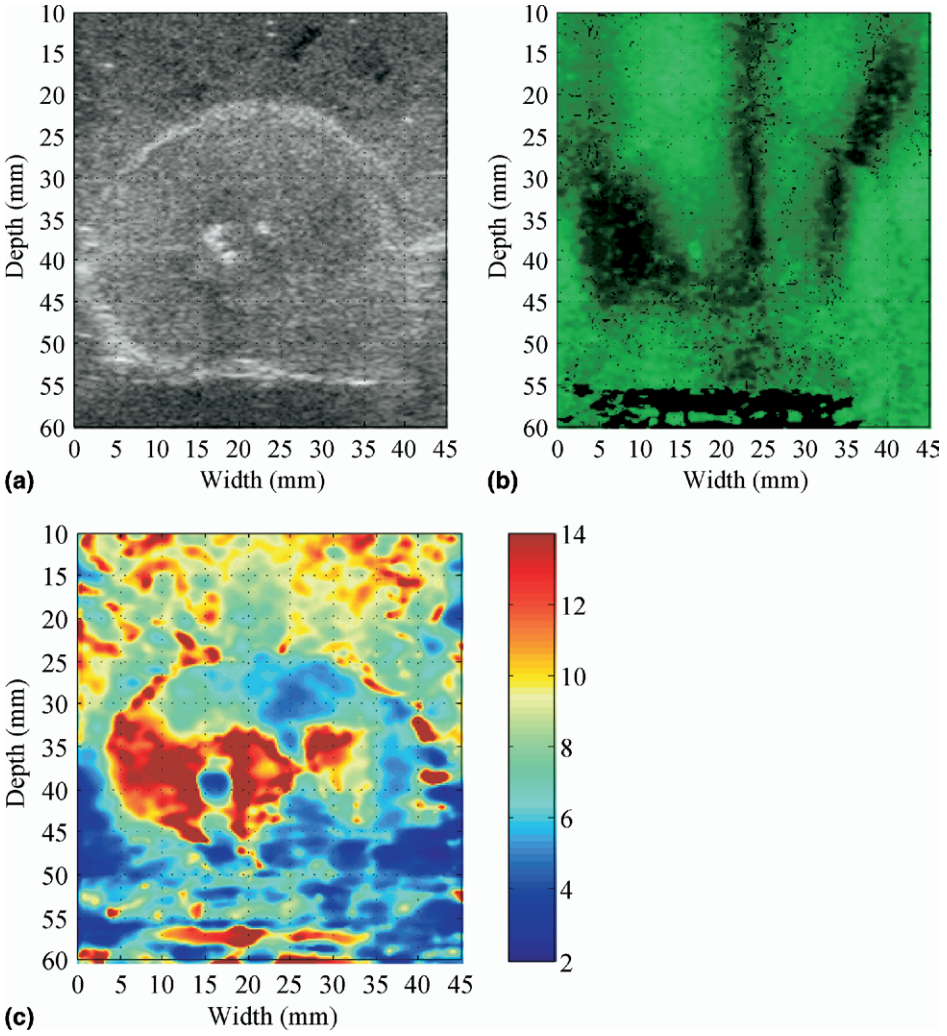

Fig. 11. Experimental crawling wave results for *in vitro* prostate using vibration sources of 240 and 240.15 Hz. Results depict the matched (a) B-mode ultrasound image, (b) Sonoelastogram and (c) Shear velocity image (units of m/s). Notice that (c) depicts two distinct regions (left and right at the mid-gland level) of elevated shear velocities, which was confirmed as focal carcinomas by pathologic assessment and not evident in the B-mode ultrasound image.

wave sonoelastogram, the shear velocity image depicts a high contrast inclusion, which agrees with that observed in the ultrasound B-mode image. Mechanical measurements from phantom samples revealed a shear velocity contrast of 1.48 (*i.e.*, elastic modulus contrast of 2.2). Analysis of the shear velocity image indicates a shear velocity contrast of 1.5, which agrees with the mechanical measurements.

Experimental shear velocity imaging results for the *in vitro* prostate case are depicted in Fig. 11. Results show the matched B-mode ultrasound image (Fig. 10a), crawling wave sonoelastogram (Fig. 10b), and shear velocity image (Fig. 10c). Notice that the shear velocity image indicates two distinct regions in the left and right gland of elevated shear velocity, which are not visualized on the B-mode ultrasound image. The pathology report confirmed these two regions as focal carcinomas. Since histologic cross-sections were not available for this prostate case, no detailed information regarding tumor size can be cited.

CONCLUSIONS

In this paper, we introduced a novel sonoelastographic technique for estimating local shear velocities from moving shear wave interference patterns termed crawling waves. By estimating the phase derivative along the shear wave propagation axis for a given image plane and kernel size (conventionally orthogonal to the Doppler ultrasound scan direction), shear velocity distributions can be quantified to reflect the true underlying tissue elasticity information. Although not a prerequisite, the use of crawling waves (*i.e.*, temporally varying spatial patterns) allows visualization of the dynamic behavior of propagating shear wave and, subsequently, shear velocity image averaging to reduce noise levels.

Simulation results analyzed the fundamental tradeoffs between various system level parameters and imaging conditions. Specifically, increasing the kernel window size (analogous to Doppler color flow processing) reduces shear velocity estimator noise but compromises spatial resolution due to the moving window estimation approach. Increasing the source vibration frequency was shown to reduce estimator variance but shear wave attenuation also increases at higher vibration frequencies owing to viscoelastic effects. Thus, a fundamental tradeoff exists for practical applications. Since attenuation effectively reduces the shear wave *SNR*, the latter was also assessed in simulation. As the results revealed, lower *SNR* levels produced substantial variability in the derived shear velocity estimates. Fortunately, in practice the shear wave *SNR* can be improved to an extent by increasing the vibrational amplitude of the sources. The effects of amplitude quantization were evaluated and the results indicated that four-bit display resolution produced more variability in the shear velocity estimates than that obtained using either eight-bit or 16-bit quantization (the last being the most accurate). Despite this fact, results indicate that any of the display resolutions evaluated are acceptable for shear velocity estimation. Hence, many of the ultrasound scanners equipped with Doppler color flow imaging and routinely used today could be modified to perform real-time shear velocity imaging.

Results from homogeneous phantoms demonstrated the ability of sonoelastographic shear velocity imaging to quantify the true underlying shear velocity distributions as verified using time-of-flight measurements. Furthermore, heterogeneous phantom results revealed the capacity for lesion detection (1 cm diameter inclusion) and shear velocity quantification as validated from mechanical measurements on phantom samples. Experimental results obtained from a prostate specimen illustrated feasibility for shear velocity imaging in tissue. More importantly, high-contrast visualization of focal carcinomas was demonstrated introducing the clinical potential of this novel sonoelastographic imaging technique.

Acknowledgments—The authors are grateful for helpful suggestions from Dr. Zhe Wu, Benjamin Castaneda and Man Zhang, and for the loan of equipment and expertise from General Electric (GE) Medical Systems. This work was supported by NIH grant 5 R01 AG16317-05.

REFERENCES

Anderson WAD, Kissane JM. Pathology: Volume 2. Missouri: C.V. Mosby Company, 1977.

Barannik EA, Girnyk A, Tovstiak V, Marusenko AI, Emelianov SY, Sarvazyan AP. Doppler ultrasound detection of shear waves remotely induced in tissue phantoms and human *in vitro*. Ultrasonics 2002;40:849–852.

Bercoff J, Tanter M, Fink M. Supersonic shear imaging: A new technique for soft tissue elasticity imaging. IEEE Trans Ultrason Ferroelec Freq Control 2004;51:396–409.

Fatemi M, Greenleaf JF. Ultrasound-stimulated vibro-acoustic spectrography. Science 1998;280:82–85.

Fung YC. Biomechanics—Mechanical properties of living tissues. New York: Springer Verlag, 1981.

Gao L, Parker KJ, Lerner RM, Levinson SF. Imaging of the elastic properties of tissue—A review. Ultrasound Med Biol 1996;22: 959–977.

Greenleaf J, Fatemi M, Insana M. Selected methods for imaging elastic properties of biological tissues. Annu Rev Biomed Eng 2003;5: 57–78.

Hall TJ, Bilgen M, Insana MF, Krouskop TA. Phantom materials for elastography. IEEE Trans Ultrason Ferroelec Freq Control 1997; 44:1355–1365.

Huang SR, Lerner RM, Parker KJ. On estimating the amplitude of harmonic vibration from the Doppler spectrum of reflected signals. J Acoust Soc Am 1990;88:310–317.

Jensen JA. Estimation of blood velocities using ultrasound—A signal processing approach. New York: Cambridge University Press, 1996.

Kasai C, Namekawa K, Koyano A, Omoto R. Real-time two-dimensional blood flow imaging using an autocorrelation technique. IEEE Trans Sonics Ultrason 1985;32:458–464.

Knutsson H, Westin CJ, Granlund G. Local multiscale frequency and bandwidth estimation. Proc IEEE Conf Image Processing 1994;1: 36–40.

Landau LD, Lifshitz EM. Theory of elasticity. New York: Elsevier Butterworth-Heinemann, 1986.

Lerner RM, Parker KJ, Holen J, Gramiak R, Waag RC. Sonoelasticity: Medical elasticity images derived from ultrasound signals in mechanically vibrated targets. Acoust Imaging 1988;16:317–327.

Lizzi F, Muratore R, Deng CX, Ketterling JA, Alam SK, Mikaelian S, Kalisz A. Radiation-force technique to monitor lesions during ultrasonic therapy. Ultrasound Med Biol 2003;29:1593–1605.

Manduca A, Muthupillai R, Rossman PJ, Greenleaf JF, Ehman RL. Image processing for magnetic resonance elastography. Proc SPIE 1996;2710:616–623.

Marple SL. Computing the discrete-time analytic signal via FFT. IEEE Trans Signal Proc 1999;47:2600–2603.

McLaughlin J, Parker KJ, Renzi D, Wu C. Shear Wavespeed recovery using moving interference patterns obtained in sonoelastography experiments. J Acoust Soc Am 2006 (in press).

Nightingale KR, Palmeri ML, Nightingale RW, Trahey GE. On the feasibility of remote palpation using acoustic radiation force. J Acoust Soc Am 2001;110:625–634.

O'Donnell M, Skovoroda AR, Shapo BM, Emelianov SY. Internal displacement and strain imaging using ultrasonic speckle tracking. IEEE Trans Ultrason Ferroelec Freq Control 1994;41:314–325.

Ophir J, Céspedes EI, Ponnekanti H, Yazdi Y, Li X. Elastography: A quantitative method for imaging the elasticity of biological tissues. Ultrason Imaging 1991;13:111–134.

Ophir J, Alam SK, Garra B, Kallel F, Konofagou E, Krouskop T, Varghese T. Elastography: ultrasonic estimation and imaging of the elastic properties of tissues. Proc Instn Mech Engrs 1999;213:203–233.

Parker KJ, Huang SR, Musulth RA, Lerner RM. Tissue response to mechanical vibrations for sonoelasticity imaging. Ultrasound Med Biol 1990;16:241–246.

Parker KJ, Lerner RM. Sonoelasticity of organs: Shear waves ring a bell. Ultrasound Med Biol 1992;11:387–392.

Parker KJ, Fu D, Gracewski SM, Yeung F, Levinson SF. Vibration sonoelastography and the detectability of lesions. Ultrasound Med Biol 1998;24:1937–1947.

Sugimoto T, Ueha S, Itoh K. Tissue hardness measurement using the radiation force of focused ultrasound. Proc IEEE Ultrason Symp 1990;1:1377–1380.

Taylor LS, Porter BC, Rubens DJ, Parker KJ. Three-dimensional sonoelastography: Principles and practices. Phys Med Biol 2000; 45:1477–1494.

Taylor LS, Richards MS, Moskowitz AJ, Lerner AL, Rubens DJ, Parker KJ. Viscoelastic effects in sonoelastography: Impact on tumor detectability. IEEE Ultrason Sympos 2001;1639–1642.

Taylor LS, Rubens DJ, Porter BC, Wu Z, Baggs RB, di Sant'Agnese PA, Nadasdy G, Pasternack D, Messing EM, Nigwekar P, Parker KJ. Prostate cancer: Three dimensional sonoelastography for *in vitro* detection. Radiology 2005;237:981–985.

Wu Z, Taylor LS, Rubens DJ, Parker KJ. Sonoelastographic imaging of interference patterns for estimation of the shear velocity of homogeneous biomaterials. Phys Med Biol 2004;49:911–922.

Wu Z, Hoyt K, Rubens DJ, Parker KJ. Sonoelastographic imaging of interference patterns for estimation of shear velocity distribution in biomaterials. J Acoust Soc Am 2006;120:535–545.